Noncontact Sub-10 nm Temperature Measurement in Near-Field Laser Heating

Yanan Yue, Xiangwen Chen, and Xinwei Wang*

Department of Mechanical Engineering, Iowa State University, 2025 Black Engineering Building, Ames, Iowa 50011-2161, United States.

T he development of scanning probe microscopy (SPM) techniques, including the scanning tunneling microscope (STM), atomic force microscope (AFM), and near-field scanning optical microscope (NSOM), has made it possible for high-resolution imaging and property measurement of surfaces at micro/nanoscales.[1,2] Many studies have focused on the near-field effect involved in these systems, and an external laser is often also used in these studies, which is known as apertureless NSOM. With the help of laser energy, a high-intensity nanoscale optical field can be achieved and top-down nanofabrication becomes feasible.[3] In the apertureless NSOM, the laser beam directly irradiates the tip, which acts as an antenna to collect the laser energy and then as an emitting antenna to result in enhancement of an optical field at nanoscales.[4,5]

The enhanced optical field plays an important role in the tip—sample system analysis. First, the enhanced optical field will greatly enhance the photon—atom interaction, which boosts the scattering of the photon from the sample. Usually, the intensity of the optical field can be enhanced by orders of magnitude,[6] and the enhanced photon scattering from the sample contains much useful information, such as the Raman signal, which is known as tip-enhanced Raman scattering (TERS).[1,7] Second, the enhanced optical field in the near surface region would induce local heating beneath the tip. This heating can be of high intensity, on the order of 10 nm depth.[6] Because of the same role played in terms of the optical field enhancement, the AFM is often used alternatively in the apertureless NSOM system.[5] In this system, the tip and the sample are so close to be considered in contact with each other. Therefore, any thermal expansion from the tip and the sample induced by the local laser heating will result in

ABSTRACT An extremely focused optical field down to sub-10 nm in an apertureless near-field scanning optical microscope has been used widely in surface nanostructuring and structure characterization. The involved sub-10 nm near-field heating has not been characterized quantitatively due to the extremely small heating region. In this work, we present the first noncontact thermal probing of silicon under nanotip focused laser heating at a sub-10 nm scale. A more than 200 °C temperature rise is observed under an incident laser of 1.2×10^7 W/m^2, while the laser polarization is well aligned with the tip axis. To explore the mechanism of heating and thermal transport at sub-10 nm scale, a simulation is conducted on the enhanced optical field by the AFM tip. The high intensity of the optical field generated in this region results in nonlinear photon absorption. The optical field intensity under low polarization angles ($\sim 10^{14}$ W/m^2 within 1 nm region for 15° and 30°) exceeds the threshold for avalanche breakdown in silicon. The measured high-temperature rise is a combined effect of the low thermal conductivity due to ballistic thermal transport and the nonlinear photon absorption in the enhanced optical field. Quantitative analysis reveals that under the experimental conditions the temperature rise can be about 235 and 105 °C for 15° and 30° laser polarization angles, agreeing well with the measurement result. Evaluation of the thermal resistances of the tip—substrate system concludes that little heat in the substrate can be transferred to the tip because of the very large thermal contact resistance between them.

KEYWORDS: sub-10 nm · thermal probing · near-field laser heating · ballistic thermal transport

measurement instability.[1] Consequently, it is critical to explore the thermal response of the tip and the sample, especially the thermal expansion of the sample surface. Much research has focused on the study of the heating effect on the tip because of its small volume for the heat capacity while ignoring that in the sample, which is considered as a big sink for heat transfer.[8−10] Milner et al. studied the temperature rise of the tip heated by a pulsed laser, and they found the temperature rise could be as high as hundreds of degrees, depending on the power of the laser.[8] A similar result was also obtained in McCarthy et al.'s work.[9] As a matter of fact, the thermal response of the sample surface plays an important role because the local heating of the sample beneath the tip can also induce a considerable temperature rise. Huang et al. measured the

nanopatterning created by the pulsed laser with a resolution down to 10 nm.[3] Malkovskiy et al. estimated the temperature rise of Al substrates and pointed out that the temperature rise easily reached 100 K with even modest laser heating.[11] Baffou et al. conducted temperature mapping of nanorods by using the florescence polarization method, and Govorov et al. studied the heating effect of gold particles in a matrix.[12,13] They employed local field enhancement of a laser by small geometries to evaluate the temperature rise. The nanoparticle-induced enhancement is similar to the tip enhancement effect to some extent. To date, due to the extremely small scale of interest, no experiment has been reported on direct measurement of sample surface temperature rise induced by the nanoscale near-field laser heating in tip—substrate systems. On the other hand, such information is critical to understand photon—material interactions within sub-10 nm and the extremely localized thermal transport in surface nanostructuring and nanoscale structure characterization.

In this work we employ the Raman thermometry technique to investigate the temperature rise of the sample at sub-10 nm scales induced by the near-field heating. As an effective tool in structure analysis of materials, the Raman spectrum is an indicator of the physical and chemical properties of the material. Raman scattering is a promising tool for noncontact temperature measurement and has been applied in the study of many materials, such as silicon and carbon nanotubes (CNTs).[14,15] In Raman thermometry, the temperature can be determined by either the intensity of the Raman peak or the Raman shift, depending on the intrinsic characteristics of the material. In our previous work, we successfully measured the temperature of multiwalled carbon nanotubes (MWCNTs) using the intensity-based method and evaluated the thermophysical properties of MWCNTs.[16,17] The decision to select the intensity or the Raman shift technique depends on the peak signal of the Raman scattering and local experimental conditions. When the peak is sharp and the resolution of the spectrometer is sufficiently high, the Raman-shift-based technique is preferred, whereas if the intensity of the peak is high and quality of the measured sample is not good enough to create a sharp peak, the intensity of the peak is better for temperature measurement. In addition, if both the Stokes and the anti-Stokes peaks are available, their ratio is also good for temperature measurement.[15]

In the apertureless NSOM system, the Raman signal is greatly enhanced to a relatively high level by magnification of the optical field.[9] Theoretically, either way described above is capable of temperature measurement. However, the obtained Raman signal level depends on the incident angle and focal level. The Raman intensity can be low if the incident angle of the excitation laser is not large enough because of the

dimension limit of the setup. Zhang et al. pointed out the reduction of the local roughness of the tip induced by the heating effect would lead to signal loss in the Raman spectroscopy.[7] In addition, the intensity-based technique requires the Raman spectrometer system to be steady to ensure consistency of the measurement data. As a result, the Raman shift method is chosen for the temperature measurement in our work. The laser beam acts as both the probing tool of the Raman spectrometer and the source of the near-field heating. The Raman thermometer is employed in the temperature characterization of the silicon surface at sub-10 nm scale. Also the thermal response of the tip irritated with the laser is analyzed. To interpret the experimental result, simulation of the enhancement of the electric field in the tip—sample system is conducted and the mechanism of the temperature rise is explored.

RESULTS AND DISCUSSION

Figure 1a shows the schematic of the whole system for near-field heating and sub-10 nm temperature measurement. The Raman spectrometer is placed in front of the AFM with the laser focusing on the tip. The silicon substrate is placed beneath the Au-coated silicon tip, where the near-field heating is generated because of the tip enhancement effect. More details about the experimental setup and procedure are described in the Experimental Section. Measurement of the substrate temperature using Raman thermometry requires an established relationship between temperature and the Raman spectra. The calibration using the silicon substrate is conducted before the sub-10 nm thermal sensing experiment.

The temperature dependence of the Raman shift for the silicon has attracted much attention.[18] Balkanski et al. presented the mathematical expression of the Raman frequency change with temperature and pointed out that the relationship between frequency and temperature could be linear if the temperature rise is under 600 K.[15] Our calibration result, shown in Figure 2, provides the relationship between the Raman shift and the temperature, and the data are linearly fitted with a slope of -0.022 cm^{-1}/K, which is close to others' results from -0.02 to -0.03 cm^{-1}/K within the range 300 to 600 K.[15,18−20] In the analysis of the Raman spectrum, due to the resolution limit of the Raman spectrometer, the exact peak position cannot be determined directly from the peak position of the raw experimental data. The Gaussian function is applied on the peak fitting to get the peak position with good accuracy in the calibration.

In sub-10 nm thermal sensing, to ensure the measured temperature is from the silicon substrate under the near-field optical heating rather than from the tip, the silicon AFM tip is coated with a 20 nm thick gold (Au) layer. The optical absorption depth of Au at the
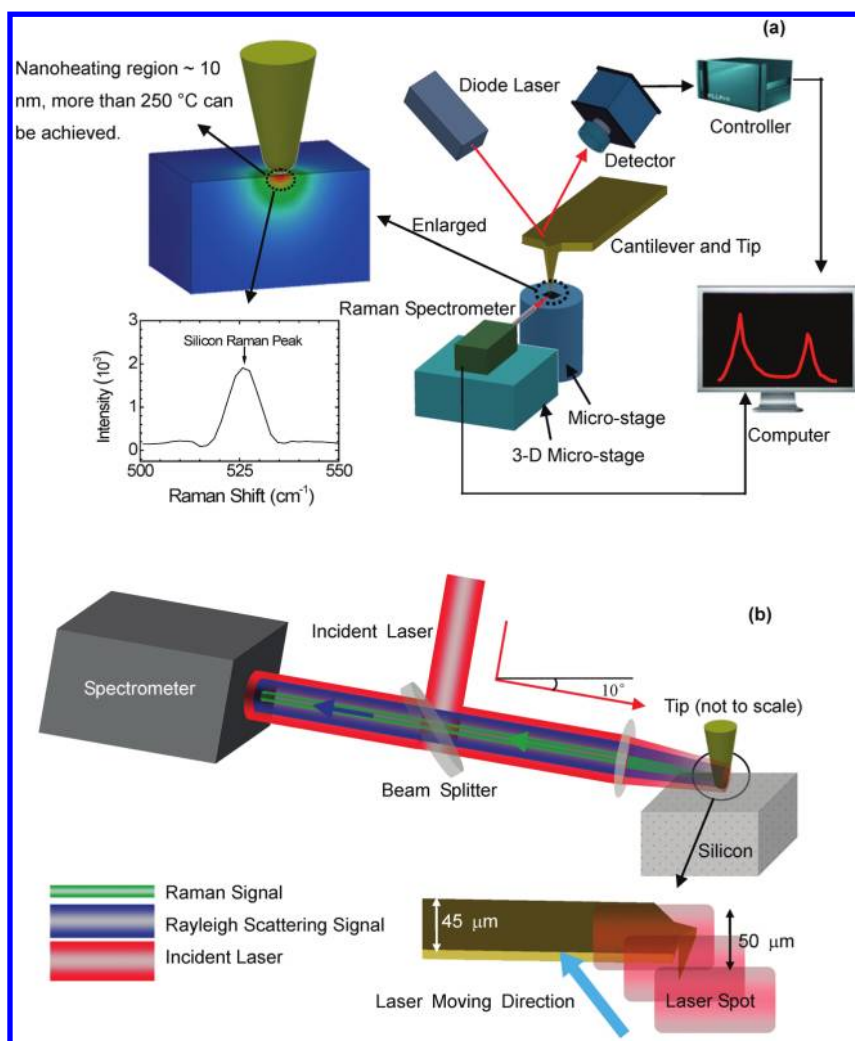
Figure 1. (a) Schematic of experimental setup for the apertureless NSOM (not to scale) for thermal sensing. Control of the cantilever and tip is accomplished by monitoring the reflection of the diode laser irradiating the cantilever. A Raman spectrometer is placed in front of the AFM, and the positions of both the Raman spectrometer and the sample are adjusted by the microstages. (b) Schematic of the optical system. The incident laser passes through a beam splitter and is focused on the tip by a convex lens. The excited Raman signal and Rayleigh scattering signal go along the same optical trace back to the spectrometer.

Raman spectrometer excitation wavelength is 13.7 nm, indicating that negligible Raman signal comes from the tip. In the experiment, three polarization angles (15°, 30°, and 75°, with respect to tip axis) of the laser are employed to induce the different near-field heating. The incident laser is moved up and down by the 3-D microstage to irradiate different parts of the tip for distinguishable near-field heating effects. The focal position is monitored by the scattered Rayleigh intensity while collecting the Raman spectrum. Because of the small projected area of the tip along the direction of laser propagation, the detected scattered intensity is always low when near-field heating occurs. The high-scattered light intensity indicates that the laser is irradiated more on the upper part and the cantilever, which is much bigger than the tip area. The schematic of this mechanism is provided in Figure 1b, and a detailed explanation is discussed in the following result analysis.

In the analysis of the Raman spectra for the substrate temperature, to be consistent with the calibration, all Raman spectra are fitted using the Gaussian function as well. Selected spectra for the three polarization angles and the fittings, shown in Figure 3, prove that good agreement is achieved between the data and fitting. The corresponding temperature of the sample is obtained by evaluating the specific Raman spectrum in the experiment against the calibration result. Variation of the substrate temperature under different laser-tip configurations (indicated by the laser scattering intensity) for three different polarization angles is shown in Figure 4.

It can be seen from Figure 4 that a temperature near 250 °C is achieved for the 15° polarization angle laser irradiation. There is not much difference between the 15° and the 30° polarizations. For the 75° polarization angle, the temperature increase is very marginal. This
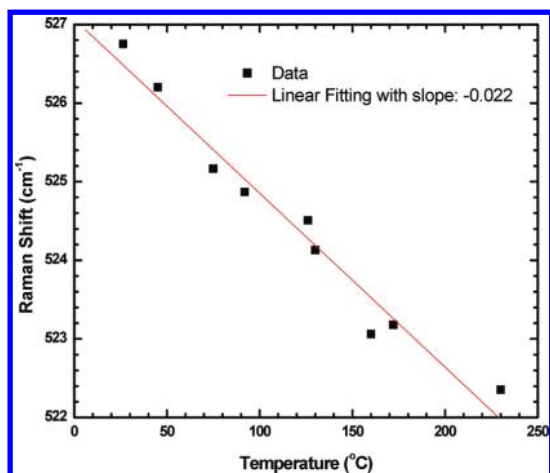
Figure 2. Calibration of the relationship between temperature and Raman shift for silicon. The slope of the linear fitting is -0.022 cm^{-1}/K.
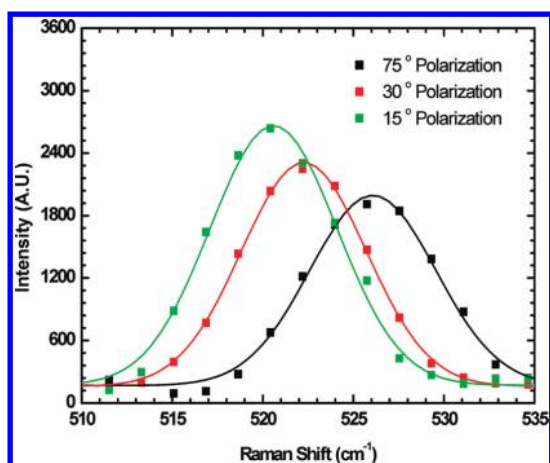

Figure 3. Selected spectra in the thermal sensing experiment. The solid lines are the Gaussian fittings for determination of the Raman peak position.
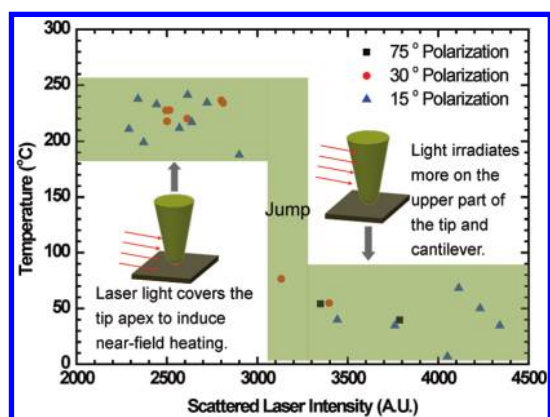

Figure 4. Measured temperature in the substrate against the scattered laser intensity. There is a jump for the temperature variation against the scattered laser intensity. The left part (high temperature) is observed when the laser covers the apex of the tip, where enhancement of electric field beneath the tip happens. The right part, where only room temperature is obtained, indicates that the laser light covers more on the upper part of the tip and the cantilever.

phenomenon can be explained by the effect of the laser polarization angle on the nanoscale optical field enhancement below the tip. In our recent work on numerical simulation of the enhanced optical field under an AFM tip, it was found that the optical field enhancement is proportional to $\cos^2 \theta$. For the 15° and 30° angles, $\cos^2 \theta$ is 0.93 and 0.75, quite close to each other. For 75°, $\cos^2 \theta$ is significantly smaller, only 0.067, meaning it is significantly weak near field focusing. The difference between 15° and 30° polarizations on near-field heating would be too small for the experiment to detect, considering effects from other factors such as the laser focusing level and the relative position between the laser and the AFM tip. However, it is found in the experiment that the 15° polarization setup is much easier to capture the Raman signal and has more data points than the other two, which explains that the smaller polarization angle induces higher enhancement for near-field focusing and heating and leads to a stronger Raman signal from the sample. In Figure 4, there is a jump (step) for the measured temperature against the scattered laser intensity (marked using a shaded area). Such phenomenon precisely reflects the laser focus on the tip apex and can be explained below. It can be seen from Figure 1b that as the laser moves from the bottom to the top, the near-field heating occurs when the laser beam covers the apex, and a large amount of the laser would pass through the tip. In this case, a high temperature rise is measured while little scattered light can be detected due to the small laser covered area. As the laser is moved up to leave the tip apex region covering the upper part of the tip and part of the cantilever, less laser would be squeezed through and the near-field optical enhancement becomes very weak, inducing little heating of the substrate. However, the scattered light intensity is highly enhanced. Since the tip is very small (only 30 nm in radius at the apex), a tiny movement of the local focal spot of the laser can make the difference between the near-field heating effect and scattered light intensity. This explains why there is a temperature jump in Figure 4 against the scattered laser intensity.

To look into the mechanism of the measured temperature rise, simulation of the electric field enhancement is conducted. A laser intensity enhancement factor as high as 3000 under the metal tip apex has been reported in the past from the multiple multipole method (MMP).[19] Recently, this method has been used to calculate the electric field distribution around a silver-coated ellipsoid.[21] Lu *et al.* estimated the near-field distribution in a tip–substrate system using the moment method.[6] Martin and Paulus adopted Green's tensor technique to simulate the electric field distribution under aperture/apertureless probes with different roughness. With the development of numerical calculations in the electromagnetic field, the finite difference in time domain (FDTD) method[2,22,23] and the

finite element method (FEM)[24−26] are widely employed due to their ability to solve more complex geometries. In this work, FEM is used to calculate the electric field distribution in the tip−substrate system.

The modeling is performed by using High Frequency Structure Simulator (HFSS V13 Ansoft, Inc.), a full-wave high-frequency 3-D finite element modeler of Maxwell's equations. The simulated model is a silicon tip whose sharp end is tangent to a hemisphere covered by an approximately 20 nm gold coating. A 200 nm
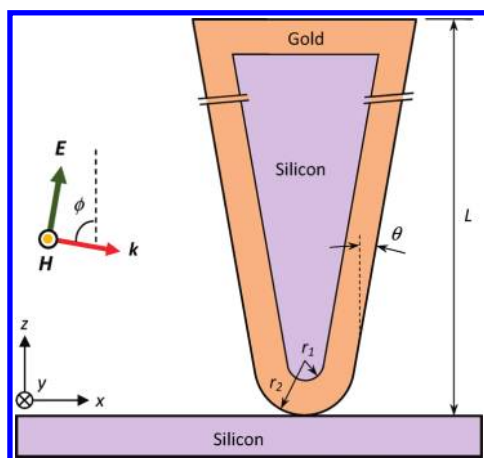

Figure 5. Schematic of tip−substrate model in the simulation. The tip with a silicon core is coated with a 20 nm thickness of gold. The geometrical parameters of the tip are as follows: half taper angle $\theta = 10°$, apex radius $r_1 = 10$ nm, $r_2 = 30$ nm, and length $L = 600$ nm. A polarized plane wave whose electric amplitude is one unit is irradiating along the x direction. The incident angle of the laser is $\phi = 80°$.

thick silicon substrate is placed normally under the tip, as shown in Figure 5. The geometry of the tip follows that used in the thermal sensing experiment discussed above: half taper angle $\theta = 10°$, apex radius $r_1 = 10$ nm, $r_2 = 30$ nm, and length $L = 600$ nm. Maxwell's equations are solved across a defined rectangular computational domain with dimensions of 800 nm × 800 nm × 900 nm, containing the tip, substrate, and vacuum around the tip/substrate. Absorbing (radiation) boundaries that stretch the boundaries infinitely far away from the structure are applied to the domain. A polarized plane wave is incident along the x direction on the tip at an angle ϕ with respect to the tip axis. The incident electric vector E has an amplitude of 1 V/m. At 785 nm (wavelength of the laser used in the experiment), the dielectric constants of gold and silicon are $\varepsilon_{Au} = -15.16 + 0.62i$, and $\varepsilon_{Si} = 13.75 + 0.06i$, respectively. Since the frequency at 785 nm is less than the plasmon frequency for gold, surface plasmon occurs on the surface of the tip. When a polarized laser illuminates a tip, the z-component of the polarized electric field drives the free electrons in the near-surface of gold and confines them to the end of the tip apex. As a result, a strong electric field arises under the tip apex.[19]

Figure 6 shows how the electric field is distributed in the tip−substrate system. It is obvious that the electric field is at low level all around except in the vicinity of the contact point, where an extremely strong electric field occurs, as shown in Figure 6a. The electric field distribution on both sides of the tip axis along the x
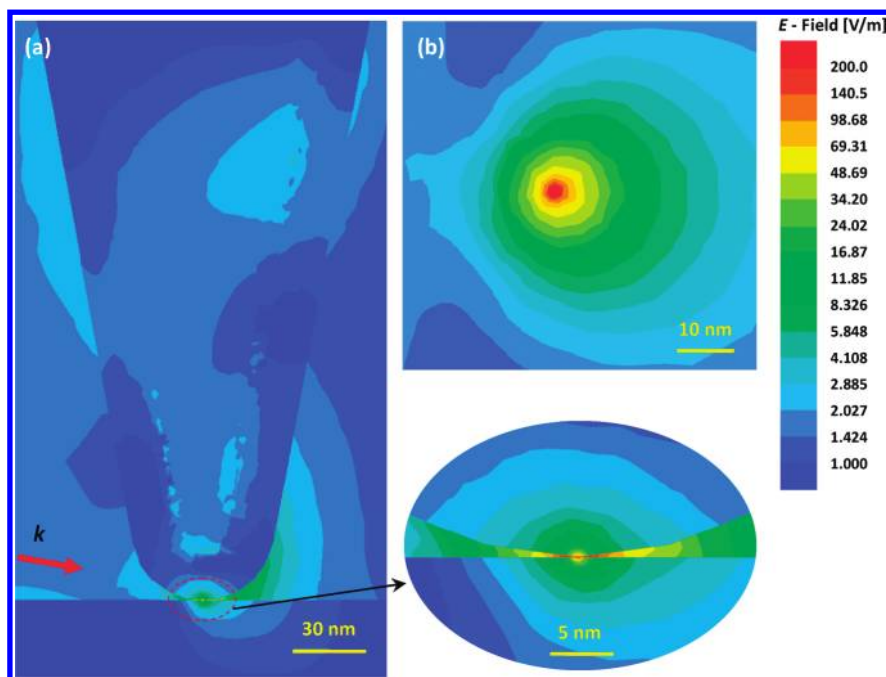

Figure 6. Electric field distribution around the tip for (a) front view in the $y = 0$ plane and (b) top view of the cross-section under the tip apex under vacuum. A strong electrical field enhancement is observed around the tip−substrate contact area. The electrical field distribution is asymmetrical around the tip, and the strong enhancement exists only in a small region of less than 10 nm.
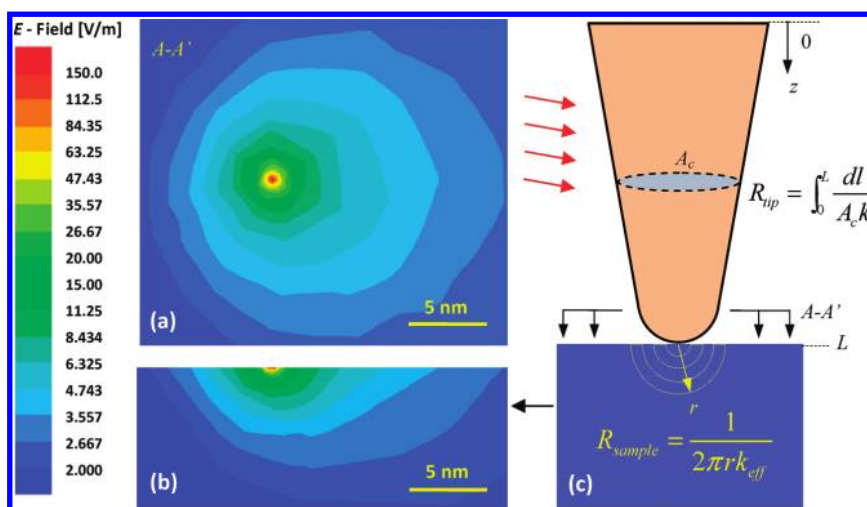
Figure 7. Electric field distribution inside the Si substrate and schematic of the thermal resistance calculation. (a) The electric field distribution in the $A–A'$ plane, (b) cross-sectional view of the distribution, and (c) schematic of the thermal resistance calculation of the tip and Si substrate. As shown in parts (a) and (b), the enhanced electric field exists only within a 10 nm region in Si and the enhancement factor can be as high as 150. Thermal resistance of the tip is calculated as 3.04×10^5 K/W by integrating l/kA_c from 0 (the apex) to L (the height of the tip). The thermal resistance of the silicon substrate is calculated by $1/2\pi r k_{eff}$ at a radius of 5 nm as 2.61×10^6 K/W. The thermal contact resistance between the tip and the substrate can be 10^{11} K/W or higher, allowing very little heat flow from the substrate to the tip.

direction is not symmetric, as in the $+x$ side the electric field amplitude is stronger than that in the counterpart position. In the top-view plane under the tip, upon moving away from the contact point, the field enhancement factor declines quickly, as shown in Figure 6b.

While most of the electromagnetic wave goes around the tip, a small portion still goes into the gold coating, even penetrating the silicon core. The silicon sample also absorbs a portion of the incident laser. A strong field enhancement is generated near the contact point both in the tip and in the sample. The field enhancement drops dramatically toward the inside of the tip and the sample, respectively, as the zoomed view shows in Figure 6. Figure 7a, b shows details of the electric field distribution in the silicon substrate. It is this electrical/optical field in the substrate that gives rise to the sub-10 nm heating. The absorption zone is almost a hemisphere (Figure 7b), with a diameter of 10 nm. In the hemispherical zone, the laser is absorbed and converted into thermal energy. The temperature of the local substrate will rise correspondingly. Comparing Figure 6 with Figure 7, it is readily found that the optical field intensity in the focused region of the silicon substrate is much stronger than that in the silicon tip (Figure 6). Considering the Raman signal from the silicon tip will be attenuated by the Au coating with a factor of $e^{-1.46}$ ($\sim$0.23), the Raman signal from the Si substrate will be orders of magnitude stronger than that from the Si tip. It is safe to conclude that the Raman signal measured in the experiment is from the Si substrate, not the Au-coated Si tip.

As shown in Figure 7a, b for the electrical field simulation result in the silicon substrate, the enhancement of the electric field has an effect only within

10 nm around the tip apex. The strong electric field within a small volume will induce intensive local heating. The heat generation rate is calculated as $Q = VI\beta$, where V is the controlled volume of interest. In this case, the calculation volume can be considered as a hemisphere. β is the absorption depth depending on the wavelength and the material. I is the irradiating energy density (W/m^2), which can be calculated from the Poynting vector equation: $I = 0.5E^2 c\varepsilon_0 n$. Here E is the intensity of the electric field, c is the light speed in a vacuum, ε_0 is the vacuum permittivity, and n is the refractive index of the medium. Applying the calculated result for the magnitude of the electric field, the energy density in Si can be calculated as a function of the incident laser intensity I_0 as $I_{Si} = (n/n_0)I_0 M^2$. In this equation, M is the magnitude of the electric field enhancement. The subscript 0 represents the vacuum conditions. Finally, the generated heat is summarized as a function of the diameter of the hemisphere and will be dissipated to the outside of the control volume through heat conduction.

To calculate the temperature rise in the near-field heating region in Si substrate, the heat transfer process can be simplified as a traditional heat conduction case for a small particle embedded in a medium, as shown in Figure 7c. The temperature can be approximated as uniform inside the near-field heating region because its dimension is extremely small ($\sim$nm). The heat transfer rate q from the heating region to the outside is equal to the heat generated from the enhanced electric field, with the thermal model established as $\int_{\Delta V} I\beta \, dv = (T - T_\infty)/R_{th}$. In this equation, the computational domain ($\Delta V \approx 2\pi r_e^3/3$) is the near-field heating region. Figure 7a, b shows this region is like an irregular

hemisphere; therefore r_e in the above correlation is the effective radius of this geometry. R_{th} is the thermal resistance from the heating region to the outside, expressed as $1/(2\pi r_e k_{eff})$, where k_{eff} is the local thermal conductivity. The above equation demonstrates that the theoretical temperature rise ($R_{th} \cdot \int_{\Delta V} I\beta dv$) of the near-field heating region can be obtained if both the electric field intensity and the thermal resistance are available. In the sections below, we will give details on how to determine the effective thermal conductivity (k_{eff}) considering the strong ballistic effect and how to evaluate the effective radius of the near-field heating region and the heating inside it.

Due to the strong ballistic heat transfer effect at small dimensions, the traditional Fourier's law of heat conduction would not be applicable for the heat conduction analysis.[27,28] When the dimension of the particle decreases to very small scale, even smaller than the mean free path of phonons, the phonon is not effective to dissipate heat to the outside since there are not enough collisions of phonons.[27] Chen pointed out that if there was not enough scattering in a small volume to build the thermal equilibrium condition, the heat conduction analysis could only be conducted using the effective thermal conductivity, which depends on the dimensionless radial distance τ ($\tau = r/\Lambda$, where Λ is the mean free path of the phonon in bulk material).[27] The the local thermal conductivity (k_{eff}) can be expressed as $3k/(3 + 4/\tau)$, where k is the thermal conductivity of bulk sample. In our experiment, the effective thermal conductivity is calculated on the basis of the mean free path of silicon as 43 nm at room temperature. The thermal conductivity of silicon within the 10 nm scale is much smaller than the bulk value.

Due to the near-field effect, the electric field under the tip was first enhanced by the incident laser. Meanwhile, the tip would be reversely excited by the enhanced electric field and contribute additional radiated electric field enhancement. Both enhancements of the electric field by the incident laser and the excited tip are second order, and meanwhile they are symmetric in the same wavelength; therefore, the overall magnitude of the intensity would be $\sim M^4$.[29] It is found that the intensity of the enhanced electric field within 1 nm in silicon is as high as 1×10^{14} W/m^2 for 15° and 30°, respectively. Although silicon is a linear optical material, this high electrical field would not just result in the one-photon, two-photon, or multiphoton absorptions, and higher level nonlinear absorption, even the avalanche ionization process, might occur. The threshold for the breakdown fluence of the avalanche process is 1×10^{13} W/m^2 for the 785 nm laser.[29] The breakdown effect always involves a very short absorption depth in the materials. For silicon, it is only 75 nm on average.[29] This short absorption depth is the result of the interaction of the laser with dense breakdown plasma. The induced electron-ion and plasma heating

would play the main role in the solid-state avalanche process.[29,30]

From the simulation result, the avalanche breakdown process happens within around 1 nm radius hemispherical region, where the electrical field intensity exceeds the threshold. Taking the calculation of 15° polarization as an example, the generated heat is calculated from the integrated electric field intensity in this region and the effective radius (r_e) is derived as 0.8 nm from the integration of volume. To compute the effective thermal conductivity, both the ballistic heat transfer effect and temperature influence on phonon transport should be considered. For bulk silicon, the thermal conductivity decreases from 148 W/(m·K) at 300 K to 98.9 W/(m·K) at 400 K.[31] The effective thermal conductivity is evaluated as 2.5 W/(m·K) in our calculation region. By applying the equation $T = R_{th} \cdot \int I\beta \, dv + T_\infty$, the theoretical temperature increases are calculated as 235 and 105 °C for the 15° and 30° cases, respectively. This first-order analysis agrees well with the measurement result. The difference could be due to the uncertainty in the first-order estimation of the ballistic thermal conductivity and approximation of the thermal transport from the non-hemispherical region. For the 75° case, a very weak enhancement effect exists and the optical field intensity is much lower than the threshold for the avalanche process. Therefore, a larger absorption depth is involved in this calculation and a negligible temperature increase occurs. Because the enhancement magnitude within a 1 nm radius region is much higher than the surroundings, its temperature rise dominates in the whole 10 nm region due to heat conduction.

In thermal response analysis of the tip, there are two sources for heating in the tip: the absorption of the direct incident laser at the upper part of the tip and the near-field heating effect in the tip apex.[8−10] All heat generated from them should be transferred up to the cantilever or down to the silicon surface. Due to the small size of the tip, the heat convection and radiation effect to the surroundings are ignored and only the heat conduction inside the tip is considered in our analysis. The heat transfer within the tip in the axial direction (z) follows the governing equation $\partial(kA_c \, \partial T \partial z)/\partial z + \dot{q} = 0$, where k and A_c are thermal conductivity and cross-sectional area, respectively, and $\dot{q}$ is the absorbed laser energy per unit length in the z direction (shown in Figure 7c). The absorbed energy comes from two sources: the direct absorption from the irradiation of the laser and the enhanced electric field due to the tip enhancement effect. For the upper part of the tip, the direct absorption from the laser predominates due to its large area, while the enhancement effect is very weak (as shown in Figure 6a). However, the scenario becomes different for the bottom part until the tip apex since the enhancement effect is relatively strong and cannot be ignored. The temperature of the tip

apex can be obtained by the integration of the above governing equation as $T_{apex} = \int_0^L [1/(kA_c) \int_z^L \dot{q}\, dz']\, dz + T_{base}$, where T_{base} is the tip temperature at the base, T_{apex} is the temperature at the apex, and L is the height of the tip ($\sim$20 μm).

Since the surface of the tip is coated with gold, which is of high reflectivity, only 3% of the laser energy is absorbed by the tip. The absorbed energy in the upper part of the tip is calculated by using the laser intensity as 1.2×10^7 W/m^2, which is the highest density of the incident laser in the experiment. In this calculation, the cantilever is assumed to be a heat sink at room temperature due to its large volume compared with the tip. Therefore, T_{base} can be regarded as room temperature. The energy density in the apex region of the tip is much higher than in the upper part due to the enhancement effect. In the simulation, the heat generated within 600 nm length from the apex of the tip is calculated as 1.4×10^{-6} W, 1.12×10^{-6} W, and 8.87×10^{-7} W for 15°, 30°, and 75°, respectively. The temperature increase at the apex of the tip is calculated to be as low as 0.7, 0.6, and 0.5 °C, respectively. The thermal conductivity used in the calculation is the value of the bulk material considering the effect of Au and Si. The real value of the thermal conductivity would be lower because of the ballistic effect at the apex of the tip and the small thickness of the gold film, which greatly reduces the mean free path of electrons in Au. Assuming the thermal conductivity is one-tenth of that used in the above calculation, the temperature increase is still less than 10 °C for all three polarizations. This indicates that there is a negligible temperature increase in the tip.

As the experiment and our numerical simulation show, the Si substrate has a higher temperature. In our experiment, the tip and the sample contact each other, and their temperature difference may result in heat transfer between them.[32] In the above discussion, the temperatures of the tip and sample are separately analyzed. The heat transfer between them will change the thermal status in the experiment. Since the temperature of the sample is higher than that of the tip, the heat transfer direction should be from the sample to the tip. As shown in Figure 7c, the direction of the thermal transport in the substrate is along the radial direction of the hemisphere from inside to the outside, and the thermal resistance is expressed as $1/(2\pi r k_{eff})$. In the calculation, because of the small region ($\sim$10 nm) of the enhancement, the temperature can be considered uniform inside the region. The effective thermal conductivity used is the value at a radius of 5 nm, and the thermal resistance of the sample is calculated as 2.61×10^6 K/W. The thermal resistance of the tip is calculated by integrating $\delta l/kA_c$ along the axial direction from 0 (the base of the tip) to L (the tip apex): $R_{tip} = \int_0^L dl/(A_c k)$. In fact, this integral does not converge, as the point at $l = L$ is a singular point. Assuming the tip

apex has a flat surface of 10 nm diameter, R_{tip} is calculated as 3.04×10^5 K/W using the thermal conductivities of bulk Si and Au. Since the tip apex is very small, the local thermal conductivity would be smaller compared with the bulk property values due to the ballistic effect of phonon/electron transport. Considering the ballistic thermal transport near the tip apex, its thermal resistance will be much higher than the aforementioned value.[33] In our experiment, because of the small volume of the tip, the contact area of the tip and the sample is very small: a circular section with a 10 nm diameter, which is a high-end estimation. As usual, the thermal resistance between hard surfaces in mechanical contact is on the order of 10^{-5} m^{2}K/W or higher. The contact resistance could be as high as 10^{11} K/W. This indicates that there would be little thermal transport between the tip and the sample. Such a phenomenon has been observed in Nakabeppu *et al.*'s experimental work. They found that there was little heat flow from a heated substrate to the tip because of the high contact resistance between them. They increased the contact area by depositing a small epoxy droplet at the tip apex in order to observe a significant temperature rise of the tip.

In our experiment, before we conducted the near-field Raman spectroscopy, we also tried to detect the surface Raman signal while the AFM tip did not approach (far from) the surface. No Raman signal was detected. We also have conducted near-field simulations for various tip–substrate gaps. It is found that if the tip is not in contact with the substrate, the electrical field intensity in the substrate quickly decreases even when the tip is moved away from the substrate by a very small distance (say, 0.1 nm). The modeling shows that if the tip is just a few nanometers away from the substrate, the enhanced electrical field in the Si substrate will be very weak and no near-field heating can be found in the substrate. It will be of great interest to study how the tip–substrate distance affects the Raman signal and heating level. This type of experimental work will be more feasible if the gap is controlled within a few nanometers while the change in the gap is controlled to be around 0.1 nm or smaller in order to capture the high sensitivity of near-field heating and the Raman signal to the tip–substrate distance.

CONCLUSION

In summary, the thermal response of a Si substrate under near-field laser heating in the apertureless NSOM was directly probed down to sub-10 nm based on Raman thermometry. The results showed that the temperature of silicon in the sub-10 nm region was as high as 250 °C for 15° and 30° polarization lasers with respect to the tip axis. A temperature jump was observed against the scattered laser light from the AFM tip, explaining that the measured high temperature was due to the laser focusing on the tip apex. The

thermal response of the tip and sample was studied by simulating the electrical field distribution around/inside them upon laser irradiation and analyzing the thermal coupling between them. The thermal contact resistance between the tip and the substrate is much higher than that of the substrate, allowing little heat conduction between them. When the laser beam polarization is well aligned with the AFM tip axis (15° and 30° angle), the optical field intensity in the sub-10 nm region ($\sim$1 $\times$ 10^{14} W/m^2 in 1 nm region) in

silicon exceeded its threshold for avalanche ionization. Taking into account this effect and the ballistic thermal transport around the nanoscale heated region, quantitative analysis gave temperature rises of 235 and 105 °C for 15° and 30° cases, agreeing well with the measurement result. The difference could be due to the uncertainty in the first-order estimation of the ballistic thermal conductivity and approximation of the thermal transport from the non-hemispherical region.

EXPERIMENTAL SECTION

In the thermal response calibration, an electric heater with controlled power is employed to heat the silicon sample from room temperature up to 230 °C, which is measured by using a T-type thermocouple attached close to the sample on the heater. The probing laser for the Raman spectrometer is 785 nm in wavelength with 62 mW output. An integration time of 10 s is used in the Raman spectrum measurement. In the laser-assisted AFM, the AFM is operated in contact mode. A silicon AFM tip of 20 μm length and 7 μm width and coated with 20 nm thick gold is attached to a cantilever, which is mounted on a 3-D microstage for fine adjustment (the tip including the cantilever is not mounted on a microstage). As shown in Figure 1a, the silicon substrate is placed on a 3-D microstage under the apex of the tip. The same laser asused in the calibration is used, and the laser beam passes through a beam splitter and a focal lens to irradiate the tip to induce near-field heating and enhanced Raman signal. A B&W Tec Raman spectrometer with a resolution of 1–2 cm^{-1} is placed in front of the AFM to detect the Raman signal. In the experiment, the spectrometer and the laser are integrated together, being placed on another 3-D stage, which can be adjusted to change the focal position of the laser beam to provide different laser focusing on the tip. To prevent signals directly from the unheated area of the silicon film, the incident angle of the laser beam was kept very small (80° with respect to the tip axis). At this very small angle, all laser beam irradiated on the sample directly can be regarded to be reflected, without generating a sensible Raman signal. The focal positions of the laser and the cantilever are monitored by the CCD camera to ensure the different focal levels in the experiment. The integration time is increased to 240 s, and the background signal is subtracted to obtain sound Raman spectra. The scattered laser beam is collected at the same time when the Raman signal is measured and is compared with the Raman signal. In the experiment, three different polarization angles (15°, 30°, 75°) are used for checking the effect of the polarization on the sub-10 nm substrate heating. Selection of the polarization angle in the experiment is limited by the polarization of the laser beam relative to the side of the spectrometer case. The intensity of the enhanced electric/optical field is directly related to the incident laser, and the enhancement depends on its polarization with respect to the tip axis. The whole setup is placed on an optical table to reduce vibration and avoid a shift of the system configuration during the experiment.

As shown in Figure 1b for the optical trace, the incident laser passes through a beam splitter and is focused on the tip by a convex lens. The excited Raman signal and Rayleigh scattering signal go along the same optical trace back to the spectrometer. The optical components are installed in a metal tube to ensure good signal-to-noise ratio, and the whole setup is placed on a 3-D microstage to make the focal point adjustable. The cantilever has dimensions of 450 μm $\times$ 45 μm $\times$ 2 μm for the length, width, and thickness, respectively. The focal point of the laser has dimensions of 100 μm $\times$ 50 μm. The large size of the laser beam allows it to cover different positions of the tip−cantilever

system. The scattered Rayleigh signal provides an effective way to monitor the focal position.

REFERENCES AND NOTES

1. Grafstrom, S. Photoassisted Scanning Tunneling Microscopy. *J. Appl. Phys.* **2002**, *91*, 1717–1753.
2. Chimmalgi, A.; Grigoropoulos, C. P.; Komvopoulos, K. Surface Nanostructuring by Nano-/femtosecond Laser-assisted Scanning Force Microscopy. *J. Appl. Phys.* **2005**, *97*, 104319.
3. Huang, S. M.; Hong, M. H.; Lukyanchuk, B. S.; Zheng, Y. W.; Song, W. D.; Lu, Y. F.; Chong, T. C. Pulsed Laser-assisted Surface Structuring with Optical Near-field Enhanced Effects. *J. Appl. Phys.* **2002**, *92*, 2492–2500.
4. Wang, X.; Lu, Y. Solidification and Epitaxial Regrowth in Surface Nanostructuring with Laser-assisted Scanning Tunneling Microscope. *J. Appl. Phys.* **2005**, *98*, 114304.
5. Wang, X. Large-scale Molecular Dynamics Simulation of Surface Nanostructuring with A Laser-assisted Scanning Tunnelling Microscope. *J. Phys. D: Appl. Phys.* **2005**, *38*, 1805–1823.
6. Lu, Y. F.; Mai, Z. H.; Chim, W. K. Electromagnetic Calculations of the Near Field of a Tip under Polarized Laser Irradiation. *Jpn. J. Appl. Phys.* **1999**, *38*, 5910–5915.
7. Zhang, W.; Schmid, T.; Yeo, B.-S.; Zenobi, R. Near-Field Heating, Annealing, and Signal Loss in Tip-Enhanced Raman Spectroscopy. *J. Phys. Chem. C* **2008**, *112*, 2104–2108.
8. Milner, A. A.; Zhang, K.; Garmider, V.; Prior, Y. Heating of an Atomic Force Microscope Tip by Femtosecond Laser Pulses. *Appl. Phys. A: Mater. Sci. Process.* **2010**, *99*, 1–8.
9. McCarthy, B.; Zhao, Y.; Grover, R.; Sarid, D. Enhanced Raman Scattering for Temperature Measurement of a Laser-heated Atomic Force Microscope Tip. *Appl. Phys. Lett.* **2005**, *86*, 111914.
10. Sarid, D.; McCarthy, B.; Grover, R. Scanning Thermal-conductivity Microscope. *Rev. Sci. Instrum.* **2006**, *77*, 023703.
11. Malkovskiy, A. V.; Malkovsky, V. I.; Kisliuk, A. M.; Barrios, C. A.; Foster, M. D.; Sokolov, A. P. Tip-induced Heating in Apertureless Near-field Optics. *J. Raman Spectrosc.* **2009**, *40*, 1349–1354.
12. Baffou, G.; Kreuzer, M. P.; Kulzer, F.; Quidant, R. Temperature Mapping Near Plasmonic Nanostructures Using Fluorescence Polarization Anisotropy. *Opt. Express* **2009**, *17*, 3291–3298.
13. Govorov, A.; Zhang, W.; Skeini, T.; Richardson, H.; Lee, J.; Kotov, N. Gold Nanoparticle Ensembles as Heaters and

Actuators: Melting and Collective Plasmon Resonances. *Nanoscale Res. Lett.* **2006**, *1*, 84–90.

14. Konstantinović, M. J.; Bersier, S.; Wang, X.; Hayne, M.; Lievens, P.; Silverans, R. E.; Moshchalkov, V. V. Raman Scattering in Cluster-deposited Nanogranular Silicon Films. *Phys. Rev. B* **2002**, *66*, 161311.

15. Balkanski, M.; Wallis, R. F.; Haro, E. Anharmonic Effects in Light Scattering Due to Optical Phonons in Silicon. *Phys. Rev. B* **1983**, *28*, 1928–1934.

16. Yue, Y.; Eres, G.; Wang, X.; Guo, L. Characterization of Thermal Transport in Micro/nanoscale Wires by Steady-state Electro-Raman-thermal Technique. *Appl. Phys. A: Mater. Sci. Process.* **2009**, *97*, 19–23.

17. Yue, Y.; Huang, X.; Wang, X. Thermal Transport in Multiwall Carbon Nanotube Buckypapers. *Phys. Lett. A* **2010**, *374*, 4144–4151.

18. Hart, T. R.; Aggarwal, R. L.; Lax, B. Temperature Dependence of Raman Scattering in Silicon. *Phys. Rev. B* **1970**, *1*, 638–642.

19. Novotny, L.; Bian, R. X.; Xie, X. S. Theory of Nanometric Optical Tweezers. *Phys. Rev. Lett.* **1997**, *79*, 645–648.

20. Chen, Y.; Peng, B.; Wang, B. Raman Spectra and Temperature-Dependant Raman Scattering of Silicon Nanowires. *J. Phys. Chem. C* **2007**, *111*, 5855–5858.

21. Bailo, E.; Deckert, V. Tip-enhanced Raman Scattering. *Chem. Soc. Rev.* **2008**, *37*, 921–930.

22. Goncharenko, A. V.; Dvoynenko, M. M.; Chang, H.-C.; Wang, J.-K. Electric Field Enhancement by a Nanometer-scaled Conical Metal Tip in the Context of Scattering-type Near-field Optical Microscopy. *Appl. Phys. Lett.* **2006**, *88*, 104101.

23. Wang, Z. B.; Luk'yanchuk, B. S.; Li, L.; Crouse, P. L.; Liu, Z.; Dearden, G.; Watkins, K. G. Optical Near-field Distribution in an Asymmetrically Illuminated Tip−sample System for Laser/STM Nanopatterning. *Appl. Phys. A: Mater. Sci. Process.* **2007**, *89*, 363–368.

24. Shi, J.; Lu, Y. F.; Cherukuri, R. S.; Mendu, K. K.; Doerr, D. W.; Alexander, D. R.; Li, L. P.; Chen, X. Y. Laser-assisted Nanoscale Deposition of Diamond-like Carbon Films on Tungsten Tips. *Appl. Phys. Lett.* **2004**, *85*, 1009–1012.

25. Zhang, W.; Cui, X.; Martin, O. J. F. Local Field Enhancement of an Infinite Conical Metal Tip Illuminated by a Focused Beam. *J. Raman Spectrosc.* **2009**, *40*, 1338–1342.

26. Zhang, J.; Skomski, R.; Lu, Y. F.; Sellmyer, D. J. Temperature-dependent Orbital-moment Anisotropy in Dilute Magnetic Oxides. *Phys. Rev. B* **2007**, *75*, 214417.

27. Chen, G. Nonlocal and Nonequilibrium Heat Conduction in the Vicinity of Nanoparticles. *J. Heat Transfer* **1996**, *118*, 539–545.

28. Siemens, M. E.; Li, Q.; Yang, R.; Nelson, K. A.; Anderson, E. H.; Murnane, M. M.; Kapteyn, H. C. Quasi-ballistic Thermal Transport from Nanoscale Interfaces Observed Using Ultrafast Coherent Soft X-ray Beams. *Nat. Mater.* **2010**, *9*, 26–31.

29. Downes, A.; Salter, D.; Elfick, A. Finite Element Simulations of Tip-Enhanced Raman and Fluorescence Spectroscopy. *J. Phys. Chem. B* **2006**, *110*, 6692–6698.

30. McFeely, F. R.; Cartier, E.; Terminello, L. J.; Santoni, A.; Fischetti, M. V. Soft-x-ray-induced Core-level Photoemission as a Probe of Hot-electron Dynamics in SiO_2. *Phys. Rev. Lett.* **1990**, *65*, 1937.

31. Incropera, F. P.; DeWitt, D. P.; Bergman, T. L.; Lavine, A. S. *Fundamentals of Heat and Mass Transfer*; John Wiley & Sons, Inc.: New York, 2007; p 931.

32. Depasse, F.; Gomès, S.; Trannoy, N.; Grossel, P. AC Thermal Microscopy: a Probe-sample Thermal Coupling Model. *J. Phys. D: Appl. Phys.* **1997**, *30*, 3279–3285.

33. Nakabeppu, O.; Chandrachood, M.; Wu, Y.; Lai, J.; Majumdar, A. Scanning Thermal Imaging Microscopy Using Composite Cantilever Probes. *Appl. Phys. Lett.* **1995**, *66*, 694–696.